Interfacial Dislocation Networks and Creep in Directional Coarsened Ru-Containing Nickel-Base Single-Crystal Superalloys

L.J. CARROLL, Q. FENG, and T.M. POLLOCK

Mechanisms of creep deformation in nickel-base superalloy single crystals in the directional coarsening regime have been studied in alloys with large variations in γ-γ' lattice misfit and phase composition, achieved by Ru additions and variable levels of Cr and Co. Interfacial dislocation spacings established by long-term annealing experiments under no externally applied stress indicate that the experimental alloys have high-temperature lattice misfits ranging from near-zero to as large as –0.65 pct. Variation in misfit influences the stress-induced directional coarsening (rafting) behavior during creep deformation at 950 °C and 290 MPa. In postcreep deformed material, the density of excess dislocations (defined as the dislocations beyond those necessary to relieve the lattice misfit) at the γ-γ' interfaces varied with alloy composition, with the most creep-resistant alloy containing the highest excess interfacial dislocation density. In the directional coarsening creep regime, continued deformation requires shearing of the γ' rafts and is strongly influenced by the resistance of the precipitates to shearing as well as the interfacial dislocation structure. A preliminary model for creep in the rafting regime is developed.

DOI: 10.1007/s11661-008-9520-7

I. INTRODUCTION

CONTINUED development of nickel-base single-crystal superalloys has focused on Ru additions for improvement of high-temperature capability. Higher temperatures may be achieved *via* increased resistance to precipitation of topologically close-packed (TCP) phases,[1–4] increased liquidus temperatures,[1,5] and improved high-temperature creep resistance.[3,6] Although it is generally accepted that potential benefits are possible with Ru additions, the mechanisms by which Ru improves the creep resistance and improves phase stability are not well understood. There is also conflicting evidence regarding the influence of Ru on elemental partitioning between the γ and the γ' phases, and more specifically, whether Re partitions less strongly to the matrix in the presence of Ru.[1,2,4,7–13] The influence of Ru on the γ and the γ' phase compositions is critical to the high-temperature creep resistance because the elemental partitioning governs the γ-γ' lattice misfit and the deformation resistance of the phases. Additionally, the improved resistance to precipitation of TCP phases may be explained by a better understanding of the relationship between the alloy composition and the phase compositions.

L.J. CARROLL, Lead Engineer, is with General Electric Aviation, Cincinnati, OH 45215. Contact e-mail: laura.carroll@ge.com Q. FENG was formerly Senior Research Fellow with the Department of Materials Science and Engineering, University of Michigan, Ann Arbor, MI 48109, is now Professor with the State Key Laboratory for Advanced Metals and Materials, University of Science and Technology Beijing, Beijing 100083, P.R. China. T.M. POLLOCK, L.H. and F.E. Van Vlack Professor, is with the Department of Materials Science and Engineering, University of Michigan, Ann Arbor, MI, 48109.
Manuscript submitted May 25, 2007.
Article published online April 15, 2008

During high-temperature creep of commercial superalloys, which typically have a negative lattice misfit, the γ' precipitates directionally coarsen into platelike structures or "rafts" oriented perpendicular to the externally applied tensile stress. The lattice misfit δ is defined here as

$$\delta = (a_{\gamma'} - a_{\gamma})/a_{\gamma} \quad [1]$$

where $a_{\gamma'}$ and a_{γ} are the lattice parameters of the γ' precipitate and γ matrix phase, respectively. Concurrent with rafting is the development of a three-dimensional nodal network of dislocations that stabilizes the horizontal γ-γ' interfaces and relieves the stresses due to the lattice misfit. Differences in the lattice parameters and the elastic modulus of the γ and the γ' phases provide the driving force for formation of the interfacial dislocation networks and directional coarsening of the γ' precipitates.[14,15] It is well understood that the magnitude of the lattice misfit controls the density of the interfacial dislocations required to eliminate the misfit stresses. Assuming that the network dislocations are oriented to most efficiently relieve the misfit, the lattice misfit is inversely related to the spacing of the interfacial networks (d) such that

$$d = \frac{|\mathbf{b}|}{|\delta|} \quad [2]$$

in which $|\mathbf{b}|$ is the magnitude of the edge component of the Burgers vector and δ is the lattice misfit.[16] Therefore, the average spacing of dislocations within the equilibrium interfacial networks provides a reasonably good estimate of the high-temperature lattice misfit at the temperature which they are formed.[16–18] It is generally observed, however, that the interfacial

dislocation networks that form during high-temperature creep deformation are more finely spaced than the equilibrium dislocation networks that form at high temperatures without an externally applied stress.[15,18–20] The implications of the excess dislocations present at the interface during high-temperature creep and their role in shearing of the γ' for continued deformation are also not yet well understood.

Both the rafted γ' microstructure and the interfacial dislocation network spacings are relatively stable after their formation during primary creep[15,18,21,22] and are believed to largely contribute to the creep strength at high temperatures.[15,18,23–25] The rafted microstructure eliminates a continuous path for dislocations to glide through the matrix, forcing dislocations to shear the γ' for further deformation. Additionally, the interfacial dislocation networks further interfere with shearing of the γ' rafts by resisting dislocation glide through the matrix and inhibiting dislocation glide up to the γ-γ' interface and the formation of a superdislocation for shearing of the ordered precipitate.[18,24,25] Recently, the interfacial network spacing was suggested to be the major determining factor in the overall creep resistance at 1100 °C.[25,26] On the other hand, it has also been proposed that the high-temperature creep resistance depends on a balance of properties, including the opposition of the γ' rafts to shearing.[15] Typically, single-crystal superalloys with a larger negative lattice misfit have higher creep resistance. Interestingly, while it is generally concluded that at high temperatures shearing of the γ' rafts governs the creep resistance, the associated rate-limiting dislocation mechanism for dislocations entering and gliding across the precipitates has not yet been conclusively identified. In summary, the relationship between the interfacial dislocation networks and the shearing of the γ' precipitates is not well understood, nor is the relationship between the creep strength and the interfacial dislocation networks that form during deformation.

The experimental Ru-containing single-crystal superalloys investigated in this study encompass a broad range of compositions and high-temperature lattice misfit and exhibit varying high-temperature creep behavior.[13,27] Therefore, the experimental alloy set provides the opportunity to investigate the influence of Ru additions on high-temperature creep behavior and the deformation mechanisms operating during high-temperature creep in the directional coarsening regime. This article focuses on the high-temperature creep behavior, and particularly on the interfacial dislocation networks of several experimental Ru-containing single-crystal superalloys that have a negative lattice misfit. More specifically, the relationship between the interfacial dislocation networks, high-temperature creep resistance, γ-γ' phase compositions, and the lattice misfit, all of which are influenced by the addition of Ru, will be discussed.

II. EXPERIMENTAL PROCEDURES

Polycrystalline ingots of the experimental Ru-containing nickel-base superalloys were cast by Sophisticated Alloys, Inc. (Butler, PA). The experimental alloy compositions have "second-generation" levels of Re and W and 5.7 wt pct Ru and are listed in Table I. The reference alloy for the Ru-containing experimental alloys is MK-4,[28] a modified version of the second-generation alloy, CMSX-4.[29] The polycrystalline ingots were directionally solidified into single-crystal bars (19 and 12.7 mm in diameter) in clusters of four in a laboratory-scale Bridgman furnace. Further details regarding the characterization of these alloys are published elsewhere.[13,27] The SX bars were given a solution treatment and subsequently aged at 1100 °C for 8 hours, as shown in Table II. The solution temperature and time for each alloy, determined from the differential thermal analysis curves and by microstructural analysis, resulted in less than 5 vol pct eutectic and no incipient melting.

Table I. Compositions (Weight Percent) of the Ru-Containing Experimental Single-Crystal Superalloys

Alloy	Ni	Al	Ru	Ta	Re	W	Co	Cr	Mo	Ti
UM-F19	58.8	6.0	5.7	8.1	4.5	3.0	7.2	6.7	—	—
UM-F20	63.6	6.0	5.7	8.1	4.5	3.0	2.4	6.7	—	—
UM-F22	63.2	6.0	5.7	8.0	4.5	3.0	2.4	3.4	—	—
UM-F30	56.0	6.0	5.7	8.0	4.5	3.0	10.0	6.7	—	—
MK-4	60.8	5.7	—	6.7	3.0	6.6	9.5	6.3	0.6	0.8

Table II. Solution Heat Treatments for the Experimental Ru-Containing Nickel-Base Single-Crystal Superalloys

Alloy	Solution and Aging Heat-Treatment Schedule of Single-Crystal Bars
UM-F16	1300 °C for 8 h, 1100 °C for 8 h
UM-F19	1300 °C for 8 h, 1100 °C for 8 h
UM-F20	1300 °C for 8 h, 1100 °C for 8 h
UM-F22	1300 °C for 1 h, 1320 °C for 6 h, and 1100 °C for 8 h
UM-F30	1290 °C for 8 h, 1100 °C for 8 h
MK-4	1300 °C for 2 h, 1140 °C for 1.5 h, and 870 °C for 16 h

Cylindrical buttonhead creep specimens were machined by low stress grinding techniques by Westmoreland Mechanical Testing and Research, Inc. (Youngstown, PA). The gage section of the creep specimens was 3 mm in diameter and 25.4 mm in length. Creep testing of [001]-oriented creep specimens was performed in vacuum at 950 °C and 290 MPa both for 200 hours and until rupture. A stress of 290 MPa was chosen in order to achieve a strain of approximately 1 pct in a reasonable time period, similar to second-generation commercial superalloys.[27] The degree of misorientation of the [001] direction was less than 10 deg in all creep samples.

The creep specimens were rapidly cooled under load to prevent the annealing of dislocations, except in the case of the creep rupture specimens. For the creep rupture testing of UM-F20 and MK-4, the load was removed just prior to rupture in order to preserve material in the gage section. After high-temperature deformation, the creep specimens were sliced perpendicular to the applied stress axis and mounted, polished,

and etched. The specimens were then also sliced along one of the ⟨100⟩ directions, as determined by the dendritic structure, parallel to the applied stress axis. Samples mounted transverse and longitudinal to the stress axis, from both the buttonhead and the gage section, were imaged *via* scanning electron microscopy (SEM). The backscattering electron detector (BSE) was used to differentiate between dendritic and interdendritic regions. Image analysis was then used to determine the volume fraction of γ' in the interdendritic and dendritic regions after creep deformation.

High-temperature long-time exposures were conducted on several of the experimental superalloys in order to enable transmission electron microscopy (TEM) analysis of the interfacial dislocation networks formed during high-temperature annealing (no externally applied stress). The alloys UM-F20, UM-F22, UM-F30, and MK-4 were exposed to 950 °C for 1500 hours to allow coalescence of the γ' and formation of equilibrium interfacial dislocation networks. The extended high-temperature exposure did not result in fully equilibrated γ-γ' microstructure in several of the alloys, and thus, UM-F22, UM-F30, and MK-4 were exposed at 1000 °C and then again at 1050 °C for 1000 hours.

Foils for TEM were also prepared from material cut from the gage section perpendicular and parallel to the applied stress axis from specimens crept to approximately a 1 pct strain and to rupture. For the rupture samples, material for the foils was removed at least several millimeters away from the rupture location. The samples were mechanically ground to 175 to 200 μm using a polishing wheel and then ground by hand to 100 to 110 μm. Further thinning was performed electrochemically by twin jet polishing in a solution of 68 pct methanol, 10 pct percholoric acid, 9 pct distilled water, and 13 pct butyl cellusolve by volume. The optimum jet polishing conditions were determined to be −35 °C, 20 V, and 50 mA.

A PHILIPS* CM12 scanning transmission electron microscope with a Gatan-modified PHILIPS double tilt specimen holder was used for dislocation analysis. The TEM investigation of the interfacial dislocation networks was conducted for UM-F20, UM-F22, UM-F30, and MK-4 in order to observe the structure and the spacing of the dislocation networks. Extensive **g**·**b** analysis of several typical interfacial dislocation networks was conducted. The **g**·**b** = 0 invisibility criterion was used and at least two invisibility conditions, though typically three, were required for Burgers vector analysis.

The interfacial dislocation networks were also imaged directly in the (001) zone axis to reveal the network structure, because all of the ⟨110⟩{111}-type dislocations are visible. Furthermore, imaging in the (001) zone axis was beneficial because while the dislocations lie on {111} planes, glide is arrested at the γ-γ' interface, and therefore, the dislocations are essentially perpendicular to the electron beam when the foil is oriented with the incident beam in the [001] direction. Network spacing measurements were conducted at 1 pct strain and at rupture as well as on specimens annealed at high temperature for extended times. The high-temperature lattice misfit was estimated, according to the method

*PHILIPS is a trademark of FEI Company, Hillsboro, OR.

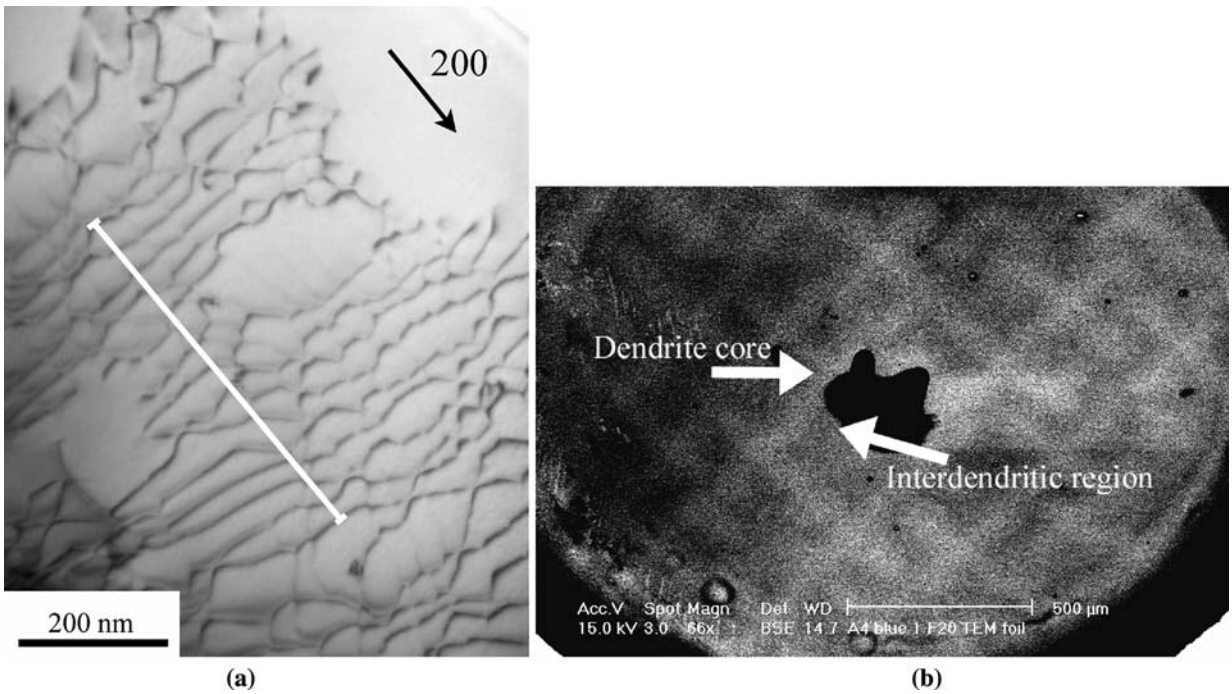

Fig. 1—(*a*) TEM image illustrating the method used to measure the interfacial dislocation spacing in two beam images from the (001) zone axis. (*b*) SEM image depicting the perforation in a TEM foil along with the existing dendritic microstructure.

used by Lahrman and co-workers,[17] from the spacing of the equilibrium interfacial dislocation networks formed during extended high-temperature annealing. Dislocation network spacing measurements were made from bright field (BF) images in a ⟨200⟩-type two-beam condition in the (001) zone axis parallel to the **g** vector, as shown in Figure 1(a). Individual spacings were measured across as many dislocation lines as practical for a given line in order to obtain a statistically representative average. The average spacing was then determined from a minimum of 50 measurements for the crept samples and a minimum of 20 measurements from the annealed samples in regions in which well-developed networks had formed.

To determine if the dislocation spacing varied between the dendritic and interdendritic regions in the crept specimens, selected TEM foils were imaged with the BSE detector in the SEM to differentiate between the dendritic and the interdendritic areas prior to TEM analysis, as shown in Figure 1(b). Measurements made from the dendritic and interdendritic regions were tracked and detailed statistical analysis was conducted in order to compare the variation in spacings between the dendritic and interdendritic regions to the variation within any given dendritic or interdendritic area. Statistical analysis comparing crept networks from selected alloys both at 1 pct creep strain and at rupture was also conducted using MINITAB software.

III. RESULTS

A. *Microstructure*

The four polycrystalline experimental alloy compositions were directionally solidified as single-crystal bars and contained no casting defects, such as freckles or misoriented grains. The average primary dendrite arm spacing of the single-crystal experimental alloys was approximately 300 μm.

Cuboidal γ' precipitates were observed following solution heat treatment and aging in UM-F19, UM-F20, UM-F30 and, as expected, in MK-4, as shown in Figures 2(a), (c), (g), and (i), respectively. The UM-F22 alloy displayed intermediately-shaped γ' precipitates, defined as precipitates with rounded corners and showing a tendency toward planar interfaces, illustrated in Figure 2(e). The γ' precipitates in the experimental alloys were approximately 300 to 400 nm in width, and the γ' volume fraction was approximately 60 pct. The volume fraction of the γ' phase in the dendritic and interdendritic region is given for the experimental alloys and MK-4 in Table III. Slight variations in the volume fraction of γ' existed between the dendrite core and the interdendritic region, such that the volume fraction of γ' was slightly higher in the interdendritic regions.

The compositional variation among the Ru-containing experimental alloys is limited to the Co and Cr contents (balanced by Ni), as shown in Table I. The UM-F19, UM-F20, and UM-F30 alloys contain 5.7 wt pct Ru and 6.7 wt pct Cr, while the Co content is 7.2 to 2.4 to

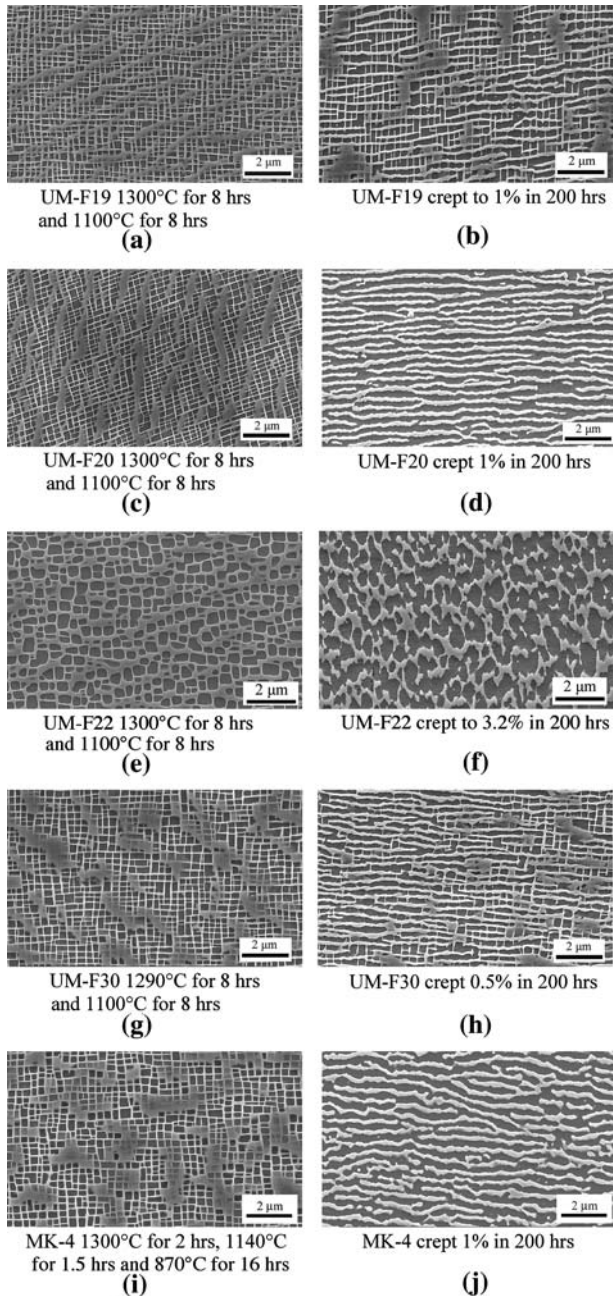

Fig. 2—SEM images of the solution-heat-treated and aged γ-γ' microstructure of (*a*) UM-F19, (*c*) UM-F20, (*e*) UM-F22, (*g*) UM-F30, and (*i*) MK-4. SEM images of the postcrept γ-γ' microstructure from the dendritic region of (*b*) UM-F19, (*d*) UM-F20, (*f*) UM-F22, (g) UM-F30, and (*i*) MK-4 alloys after creep at 950 °C and 290 MPa. The applied tensile stress is in the vertical direction and in the plane of the page.

10.0 wt pct, respectively. The UM-F22 alloy composition is based on the UM-F20 composition, but with less Cr, at 3.4 wt pct. It is also important to notice that the experimental Ru-containing alloys discussed in this article have similar levels of the potent solid solution strengtheners, approximately 8.0 wt pct Ta, 3.0 wt pct W, and 4.5 wt pct Re. Finally, the experimental alloys have equivalent amounts of Ru, which has recently been shown to improve the high-temperature creep behavior through

Table III. Volume Fraction of the γ′ Phase, Minimum Creep Rates, and Creep Rupture Lives of the Experimental Ru-Containing Single-Crystal Alloys at 290 MPa and 950 °C

Alloy	Volume Fraction of γ′		Minimum Creep Rate (s)	Rupture Life (h)
	Dendritic	Interdendritic		
UM-F19	0.57	0.63	8×10^{-9}	
UM-F20	0.58	0.64	6×10^{-9}	493
UM-F22	0.55	0.61	10×10^{-9}	347*
UM-F30	0.60	0.63	0.9×10^{-9}	869*
MK-4	~0.62		6×10^{-9}	275**

*Creep test was stopped prior to rupture.
**Creep specimen was misaligned or had an extraneous misoriented grain.

strengthening of the γ and the γ′ phases.[30] The Ru-free reference alloy, MK-4, varies slightly in composition from the Ru-containing experimental alloys, but also has a similar total amount of the solid solution strengtheners Ta, W, and Re: 16.3 wt pct, compared to 15.5 wt pct in the Ru-containing experimental alloys.

B. *Creep and Microstructural Evolution*

The creep behavior at 950 °C and 290 MPa of the single-crystal alloys was highly variable. The 200-hour creep and the creep rupture curves are shown for the experimental alloys and MK-4 in Figure 3. The experimental Ru-containing alloys with cuboidal γ′ precipitates are more creep resistant at 290 MPa and 950 °C than UM-F22, which has intermediately-shaped γ′ precipitates. The UM-F19 and UM-F20 alloys displayed similar minimum creep rates and creep behavior for the first 200 hours, though UM-F19 accumulated more strain during primary creep. The minimum creep rates and creep rupture lifetimes are shown in Table III. The UM-F30 alloy was significantly more creep resistant than the other experimental alloys and MK-4 at 290 MPa and 950 °C. The minimum creep rate of UM-F30 is approximately 0.9×10^{-9}/s, half an order of magnitude lower than the minimum creep rate of UM-F19 and UM-F20, which are 8×10^{-9}/s and 6×10^{-9}/s, respectively.

At this stress and temperature condition, the rupture life of UM-F30 is approximately 900 hours, UM-F20 had a rupture life of 493 hours, and MK-4 exhibited a substantially shorter rupture life, 275 hours. The MK-4 specimen exhibited a creep rate on the order of 10^{-9}/s, but because of the early onset of the tertiary creep regime, the rupture life was shorter than the Ru-containing experimental alloys with similar minimum creep rates. The rupture life of the MK-4 specimen may have been reduced by a misoriented grain observed in the gage section of the creep rupture specimen. The rupture lifetimes were also compared to CMSX-4 at 950 °C and 290 MPa, which has a rupture life of approximately 450 hours.[31] With the exception of UM-F22, the experimental Ru-containing alloys were generally more creep resistant under these testing conditions compared to the second-generation commercial superalloy, CMSX-4.[31] Also, notice that UM-F30 exhibited the lowest minimum creep rate and the longest time to rupture, while UM-F22 had the shortest rupture life and highest minimum creep rate.

While no instabilities in terms of precipitation of TCP phases were observed, substantial variation in the directional coarsening behavior of the γ′ precipitates was observed among the Ru-containing alloys and MK-4 following creep at 950 °C and 290 MPa, as illustrated in Figures 2(b), (d), (f), (h), and (j). The tensile stress axis is in the vertical direction in the plane of the page for the postcrept microstructures shown in Figure 2. The alloys with cuboidal precipitates raft perpendicular to the tensile stress axis, indicative of a negative lattice misfit, as expected in comparison to

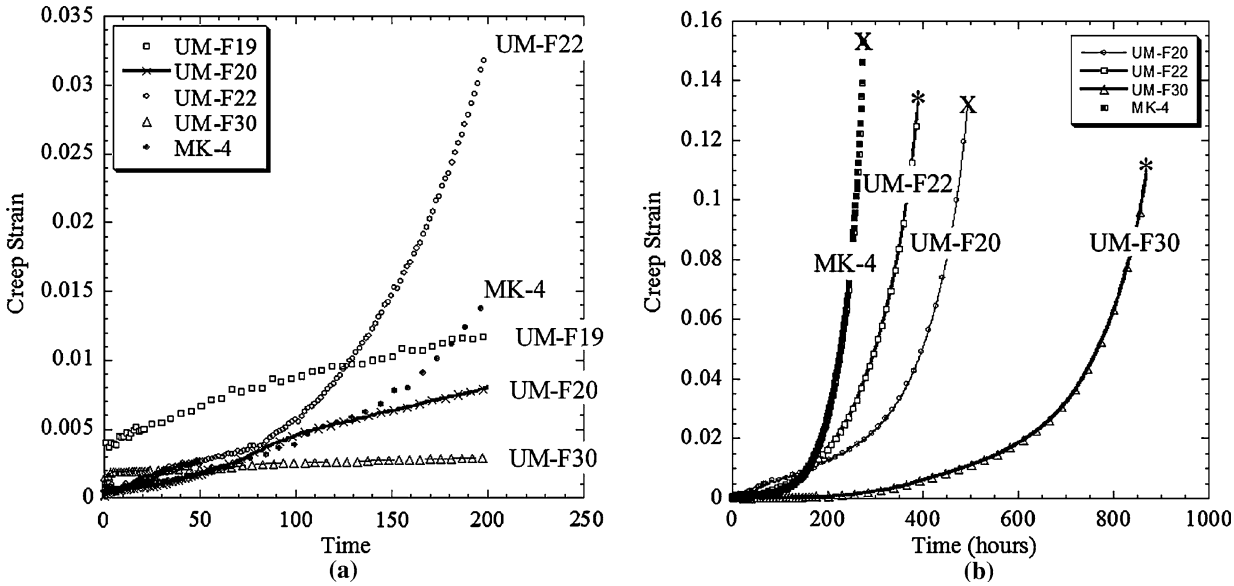

Fig. 3—Creep behavior of the experimental Ru-containing superalloys and MK-4 at 950 °C and 290 MPa for (*a*) 200 h and (*b*) until rupture. The *x* indicates that the sample failed, and * indicates the creep test was stopped prior to failure.

commercial nickel-base single-crystal superalloys. As illustrated in Figures 2(b) and (h), the rafting in UM-F19 and UM-F30 had not reached completion after 200 hours of creep at 290 MPa and 950 °C. This indicates that either the rafting kinetics of these alloys are slower or, for UM-F30, it may be the result of the lower strain accumulation during the first 200 hours (0.5 pct creep strain) relative to the other alloys (1 pct creep strain). Excess vertical γ-γ' interfaces remain in the crept γ-γ' microstructures of UM-F19 and UM-F30, while no vertical γ-γ' interfaces (with the exception of those at the ends of the γ' rafts) are observed in UM-F20 or in MK-4 after 200 hours. The UM-F30 alloy was also crept for 310 hours at 950 °C and a slightly increased stress of 310 MPa until the accumulation of 1 pct creep strain, at which time a fully rafted microstructure had developed (not shown). Recall that the UM-F20, UM-F19, and UM-F30 compositions differ only in Co content with 2.4, 7.2, and 10 wt pct, respectively.

The γ' precipitates in UM-F22 directionally coarsened into irregular rafts perpendicular to the stress axis, as illustrated in Figure 2(f). The irregular γ-γ' interfaces have a greater amount of γ-γ' interfacial area than observed for the rafts in the experimental alloys with cuboidal precipitates. This suggests that there may be a reduced driving force for the elimination of the interfacial area in UM-F22 as a result of the lattice misfit being more near zero than UM-F20, UM-F30, or MK-4. It should also be noted that in all of the experimental superalloys there was no difference between the γ-γ' microstructure of the solution-heat-treated and aged samples and the microstructure in the buttonhead of the creep specimens after creep deformation at 950 °C, indicating that limited coarsening is occurring under elastic conditions.

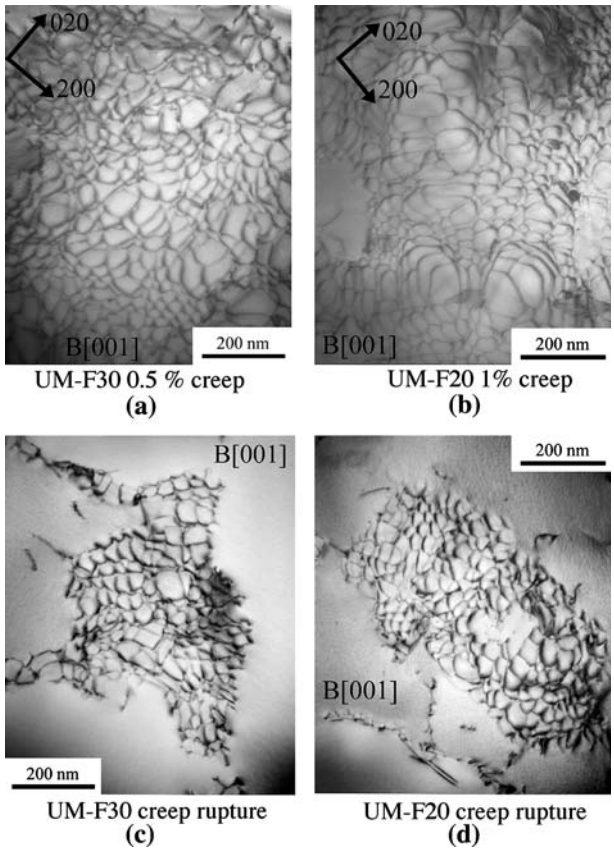

Fig. 4—BF TEM images, imaged in a multiple beam condition in the (001) zone axis, showing typical interfacial dislocation networks at (*a*) 0.5 pct creep strain in UM-F30 and (*b*) 1 pct creep strain in UM-F20; and (*c*) creep rupture in UM-F30 and (*d*) UM-F20 at 950 °C and 290 MPa.

C. *Postcrept Dislocation Substructures*

After 0.5 pct creep, 1 pct creep, and creep rupture, the interfacial dislocation networks in the alloys with cuboidal γ' precipitates, UM-F20 and UM-F30, are in mixed irregular and hexagonal configurations, as shown in Figure 4. A typical interfacial dislocation network was observed to consist locally of $\frac{1}{2}\langle 110\rangle$-type dislocations with Burgers vectors of three different types. Dislocations with Burgers vectors of all six types of $\langle 110\rangle\{111\}$ dislocations were observed over broader areas of the network. The character of the interfacial dislocation networks that formed during high-temperature creep in the Ru-containing experimental single-crystal superalloys is consistent with those observed in Ru-free commercial superalloys and MK-4.[15]

While the structural details of the interfacial dislocation networks cannot be observed from the longitudinal orientation, this view does provide insight into the dislocation densities in the γ' rafts and the γ matrix channels. Not surprisingly, longitudinal observation of the interfacial dislocation networks in UM-F20 and UM-F30 at rupture reveals that the matrix dislocations are predominately located at the γ-γ' interfaces and are associated with the interfacial networks, as shown for UM-F20 and UM-F30 in Figures 5 and 6, respectively. This observation is also consistent with Ru-free superalloys.[15] Interestingly, these BF TEM images also show that at rupture numerous dislocations were not pinned by the interfacial networks and were gliding through the matrix channels (Figures 5 through 7). Figure 7 clearly shows dislocations bowing through the γ matrix channels of UM-F20. Additionally, pairs of dislocations were commonly observed in the γ' rafts in UM-F20 and UM-F30, also shown in Figures 5 and 6, respectively. Dislocation pairs are apparent by their separation at the γ-γ' interface. The density of dislocations within the rafts in UM-F20 at rupture is approximately $10^{12}/m^2$, while the density of mobile dislocations in the γ matrix channels is somewhat higher, although approximately the same order of magnitude. Determination of the average number of dislocations in the γ and the γ' phases at rupture in UM-F30 was more difficult due to fewer TEM images in the longitudinal orientation. However, there is a similar number of dislocations in the γ' rafts at rupture in UM-F30 as in UM-F20.

As illustrated in Figure 8, the interfacial dislocation networks along the γ-γ' interfaces of irregular rafts in UM-F22 appeared to be more square than hexagonal in nature, unlike the networks in UM-F20, UM-F30, and MK-4. It is evident that the dislocation networks in UM-F22 are also substantially coarser than the

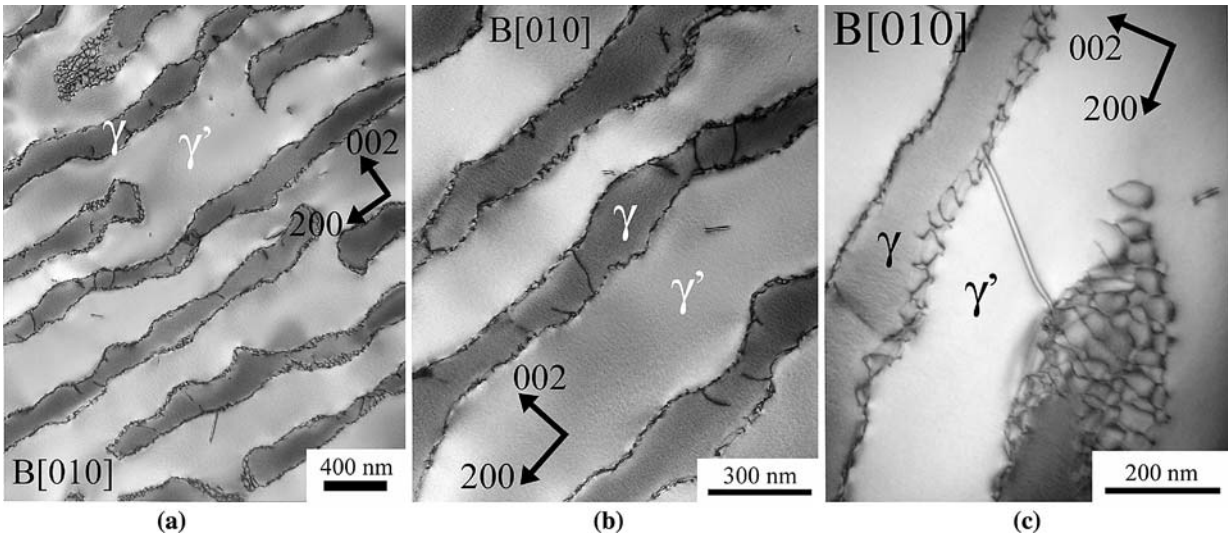

Fig. 5—BF TEM images of UM-F20 after creep rupture at 950 °C and 290 MPa imaged directly on the (010) zone axis; image is parallel to the applied stress axis. (*a*,*b*) Dislocations not associated with the interface are observed in the matrix and (*c*) pairs of dislocations are observed shearing the γ'.

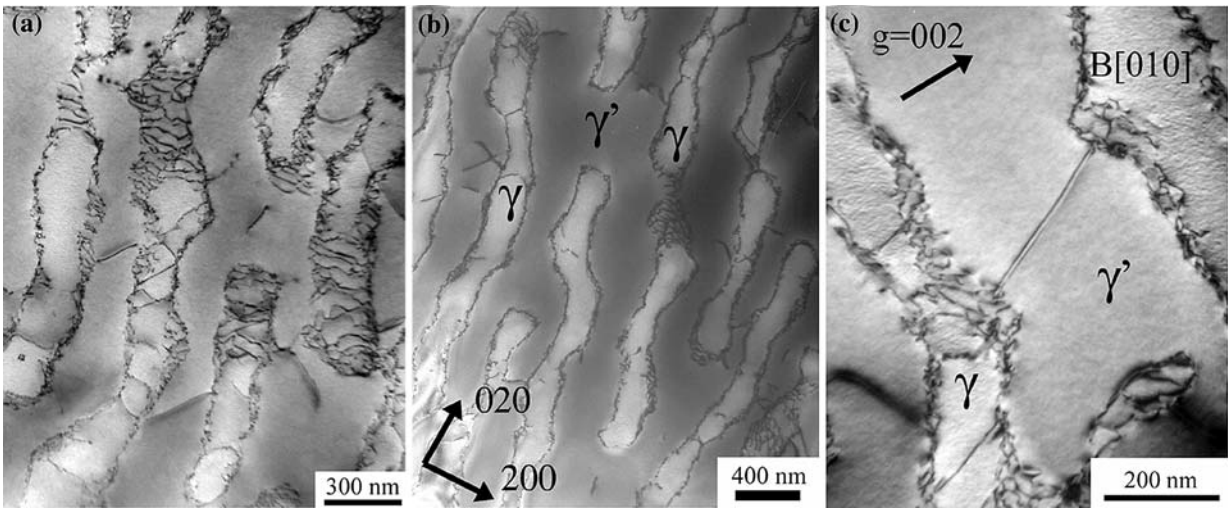

Fig. 6—BF TEM images of UM-F30 after creep rupture at 950 °C and 290 MPa in the (010) zone axis. Image is parallel to the applied stress axis.

networks in UM-F20, UM-F30, or MK-4. Interestingly, it appears that the individual γ' rafts consist of fewer coalesced γ' precipitates than observed for UM-F20, UM-F30, and MK-4, and therefore, more vertical matrix channels must be present in UM-F22. Possibly as a result of the low 1 pct creep strain at which UM-F22 was observed, there are significantly more gliding matrix dislocations observed there than for either UM-F20 or UM-F30 at rupture and, as expected, fewer dislocations were observed to be shearing the γ' phase.

D. *Postcreep Interfacial Dislocation Network Spacings*

The location within the dendritic microstructure from which each network spacing measurement was made was initially tracked at both 1 pct creep strain and at creep rupture for UM-20 and UM-F30. Statistical analysis was conducted to determine if the mean network spacing in the dendritic region differed from the mean spacing in the interdendritic regions. Statistical analysis suggested that there was not a difference between the mean spacings in dendritic and interdendritic regions.[32] Based on this finding, the reported spacings are from both regions of the dendritic microstructure.

The BF TEM images of a typical interfacial dislocation network for a $\mathbf{g} = 200$ type two-beam condition as well as the distribution of dislocation network spacings crept at 950 °C and 290 MPa to 1 pct strain and to rupture are shown for UM-F20 in Figure 9 and for UM-F30 in Figure 10. The interfacial dislocation networks at creep rupture were also investigated for MK-4 and similarly are shown in Figure 11. The network spacings

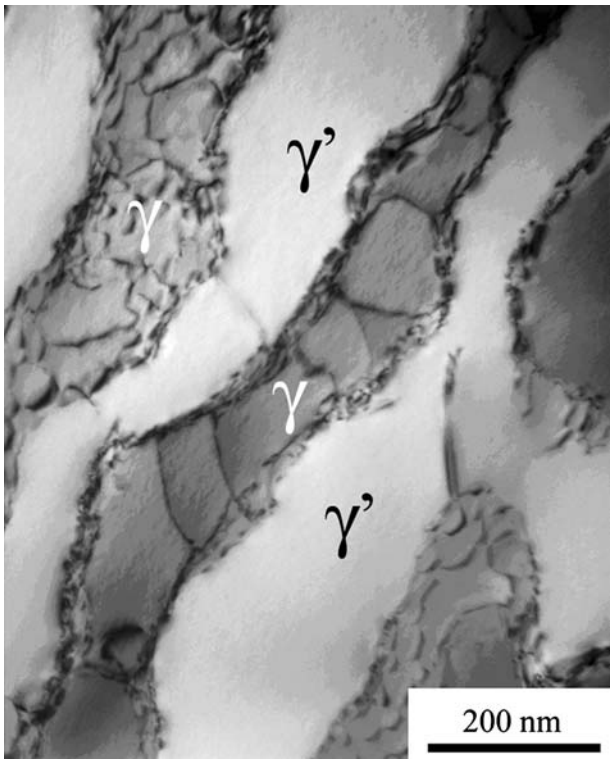

Fig. 7—TEM image viewed longitudinally of UM-F20 after creep rupture. Dislocations are observed bowing through the matrix channels.

in UM-F20, UM-F30, and MK-4 each follow a normal distribution. The mean interfacial dislocation network spacing in UM-F20 is 26 nm at 1 pct creep and 24 nm at rupture, with standard deviations of 6 and 4 nm, respectively. Slightly larger average dislocation network spacings of 32 nm at 1 pct creep and 30 nm at rupture are observed for UM-F30, with standard deviations of 6 and 5 nm, respectively. Recall that the minimum creep rate of UM-F30 is half an order of magnitude lower than UM-F20, yet surprisingly, the network spacings are not considerably different. The mean interfacial dislocation spacing in MK-4 at creep rupture was 47 nm, and thus much coarser than in the UM-F20 and UM-F30 network spacings. The interfacial dislocation spacings of each alloy at 1 pct creep strain and creep rupture are summarized in Table IV. Box plots of the distributions of the dislocation spacing measurements for UM-F20, UM-F30, and MK-4 are shown in Figure 12. The box plots clearly illustrate the large difference in the crept dislocation network spacings among the Ru-containing experimental alloys, UM-F20 and UM-F30, and the second-generation alloy, MK-4.

After 1 pct creep at 950 °C and 290 MPa, the interfacial dislocation spacing in UM-F22 was irregular and ranged between 50 and 100 nm, as shown in Figure 8. The irregularity of the γ-γ' interfaces made it difficult to obtain a representative number of measurements, and therefore, a range is reported for the network spacing. However, the dislocation network spacing in UM-F22 was coarser than in UM-F20, UM-F30, or MK-4.

E. *Equilibrium Interfacial Dislocation Network Spacings*

The magnitude of the high-temperature lattice misfit of the experimental Ru-containing superalloys, UM-F20, UM-F30, and UM-F22, and MK-4, was estimated from the spacings of the interfacial dislocation networks that developed during an extended high-temperature anneal with no externally applied stress. Efficient relief of the lattice misfit is provided by equilibrium networks formed during extended exposures at high temperatures with no applied external stresses,[15,17,18] thus the spacing of these equilibrium networks provides a reasonably accurate estimate of the γ-γ' lattice misfit at temperature.[16–18]

The γ' precipitates coalesced at different rates during high-temperature annealing of the Ru-containing experimental alloys and MK-4. Thus, to achieve fully developed networks in a reasonable time period, the aging temperature had to be increased above 950 °C for UM-F30, UM-F22, and MK-4. The γ' precipitates in UM-F20 coalesced into a rafted structure and well-developed dislocation networks formed at the γ-γ' interfaces within 1500 hours at 950 °C, as shown in Figure 13(a). The distribution of dislocation spacings in the equilibrium networks that formed at 950 °C in UM-F20 is shown in Figure 13(b). The mean equilibrium dislocation spacing of UM-F20 is 40 nm with a standard deviation of 7 nm. Assuming a Burgers vector, **b**, of 0.254 nm and using the dislocation spacing, d, of 40 nm, the magnitude of the lattice misfit $|\delta| = \frac{|\mathbf{b}|}{d}$ of UM-F20 is 0.65 pct at 950 °C.

Surprisingly, after a 1500-hour anneal at 950 °C, the size and shape of the γ' precipitates remain predominately unchanged from the solution treated and aged condition, with few dislocations observed in the matrix channels in UM-F30, UM-F22, and MK-4. Similarly, a 1000-hour anneal at 1000 °C also did not result in a rafted γ-γ' microstructure in any of the aforementioned alloys. After both extended anneals, although particularly after the 1000 °C anneal, relatively few dislocations were observed in the γ channels and they were limited to regions in which the beginning stages of precipitate coalescence was apparent. No evidence of precipitate coalescence was observed in regions devoid of dislocations.

The γ' precipitates in UM-F30 and MK-4 coalesced during the 1000-hour anneal at 1050 °C and interfacial dislocation networks developed, as shown for a two-beam condition in Figures 14(a) and 15(a), respectively. The distributions of the equilibrium network spacing measurements for UM-F30 and MK-4 are shown in Figures 14(b) and 15(b), respectively. Notice that the mean dislocation spacing of the equilibrium networks of both UM-F30 and MK-4 is 80 nm, and thus the lattice misfit is estimated as –0.3 pct (assuming a Burgers vector, **b**, of 0.254 nm). The γ' precipitates in the experimental alloy with a slightly negative misfit, UM-F22, did not exhibit significant microstructural change after 1000 hours at 1050 °C.

The average dislocation spacings of the equilibrium interfacial dislocation networks of the Ru-containing experimental alloys and MK-4 are plotted with the theoretical curve relating the magnitude of the lattice misfit and the dislocation spacing in Figure 16. The crept dislocation spacings for UM-F20, UM-F30, and

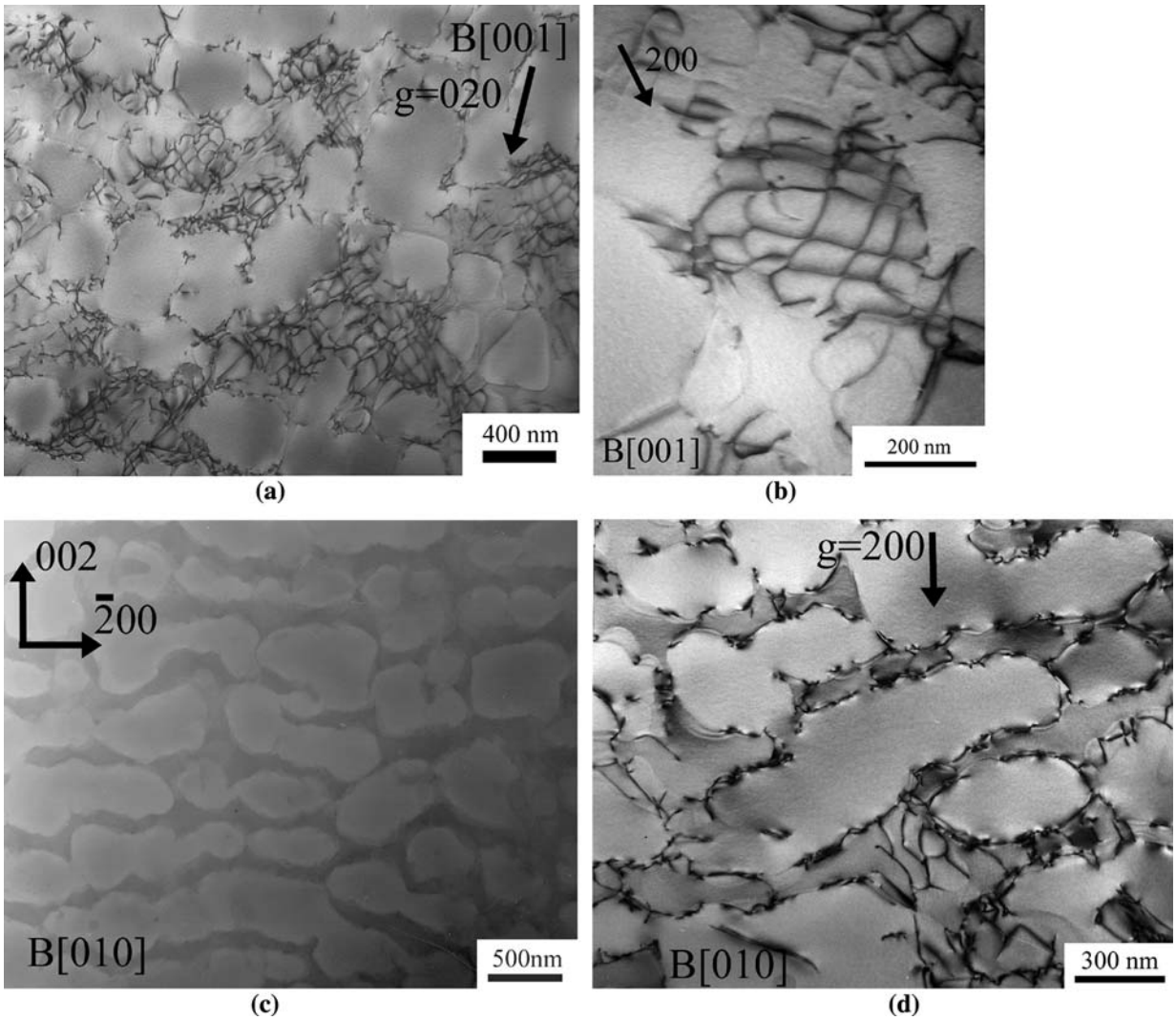

Fig. 8—(*a*) through (*d*) TEM micrographs of a typical interfacial dislocation network in UM-F22 after 1 pct creep strain at 950 °C and 290 MPa. TEM micrographs were imaged in the (001) or (010) zone axis such that all dislocation types are visible (except for in (c)).

MK-4 are also plotted according to the lattice misfit estimated from the equilibrium high-temperature dislocation networks. Therefore, the graph in Figure 16 illustrates the number of excess dislocations that exist in the interfacial networks during creep deformation relative to the misfit dislocations necessary to relieve the misfit. It is interesting to note that the most creep-resistant alloy, UM-F30, had the highest density of excess dislocations, again, defined as the density of dislocations beyond the number required to relieve the misfit. This suggests that the precipitates in this alloy are the most resistant to shearing.

IV. DISCUSSION

A. *High-Temperature Lattice Misfit*

The experimental Ru-containing superalloys in this study UM-F22, UM-F30, and UM-F20 have varying negative high-temperature lattice misfit, listed in the order of increasingly negative lattice misfit. The high-temperature lattice misfit of UM-F20 is much more negative than that of UM-F30, as well as typical second-generation commercial superalloys. From the equilibrium dislocation spacing, the lattice misfit at 950 °C of UM-F20 is estimated as –0.65 pct and as –0.3 pct for UM-F30. The high-temperature lattice misfit of second-generation commercial alloys is in the range of –0.2 to –0.3 pct[33–35] and is of similar magnitude as the third-generation superalloy, CMSX-10.[36] As expected, the lattice misfit of MK-4 was –0.3 pct and, therefore, consistent with CMSX-4 and other second-generation superalloys.[33–35] However, both MK-4 and UM-F30 have different coarsening kinetics albeit the similar lattice misfits. Somewhat surprisingly, because UM-F30 has a similar composition and amount of refractory element additions compared to UM-F20, the lattice misfit of UM-F30 at 1050 °C was much less negative than UM-F20. Recall that the only difference in composition is the Co content, 2.4 wt pct in UM-F20 and 10.0 wt pct in UM-F30 (balanced by Ni). The variation in lattice misfit between UM-F20 and

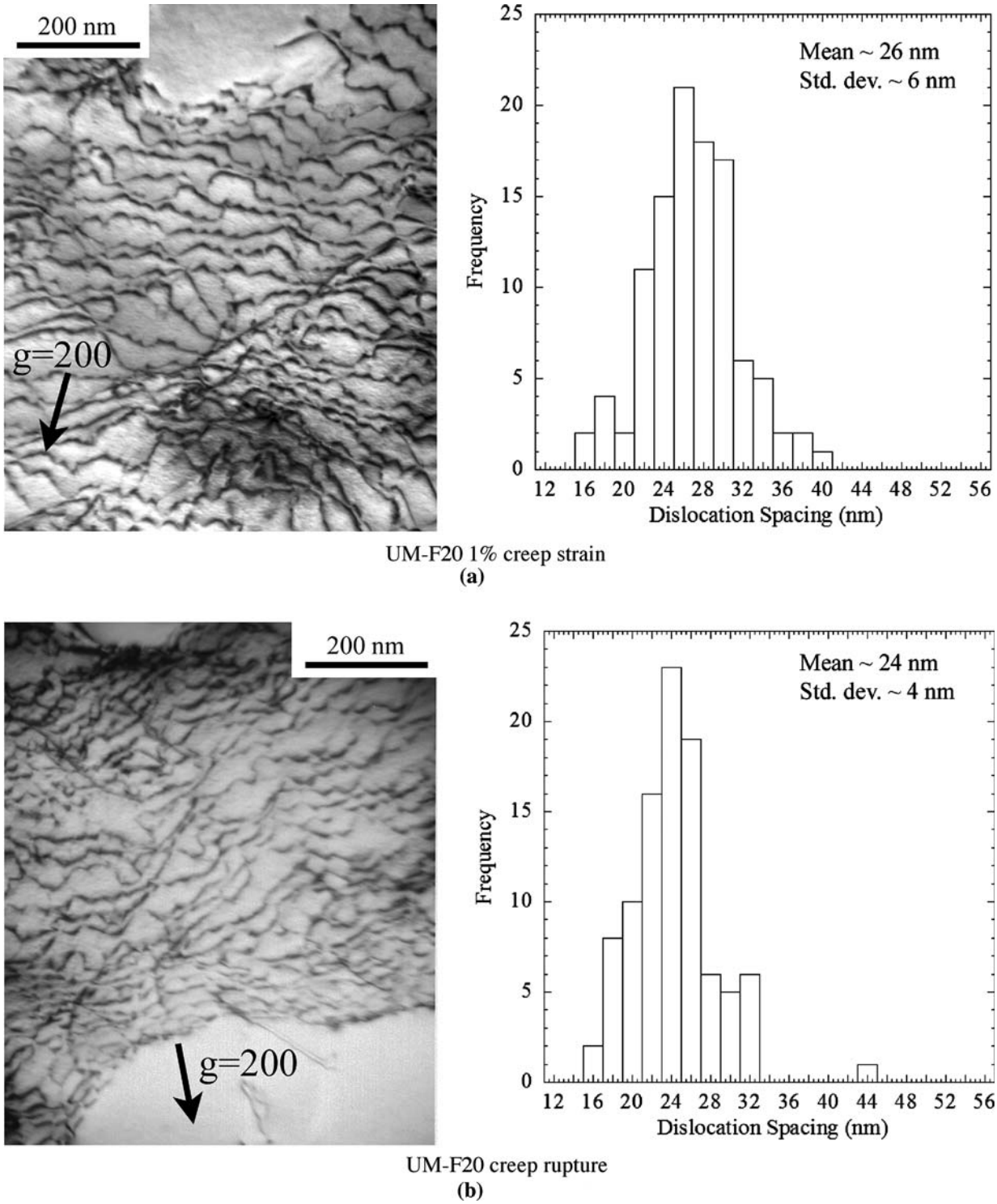

Fig. 9—TEM BF ⟨200⟩-type two-beam images from the (001) zone axis and the distribution of interfacial dislocation spacings in UM-F20 at (*a*) 1 pct creep strain and (*b*) creep rupture at 950 °C and 290 MPa.

UM-F30 suggests an effect of Co on the lattice misfit in Ru-containing experimental superalloys. The Co itself is not likely to change the lattice misfit unless it influences the partitioning of another alloying element that more strongly affects the lattice parameters. It is possible that Co may displace other elements such as Ru, Re, or W from the matrix to the precipitate, thereby reducing misfit. In the UM-F30 alloy, a higher level of Co might be expected to increase the strength of the γ' if the Ru partitioned more strongly to the precipitates with the presence of Co. Further support for Co altering partitioning is provided by Walston and co-workers,

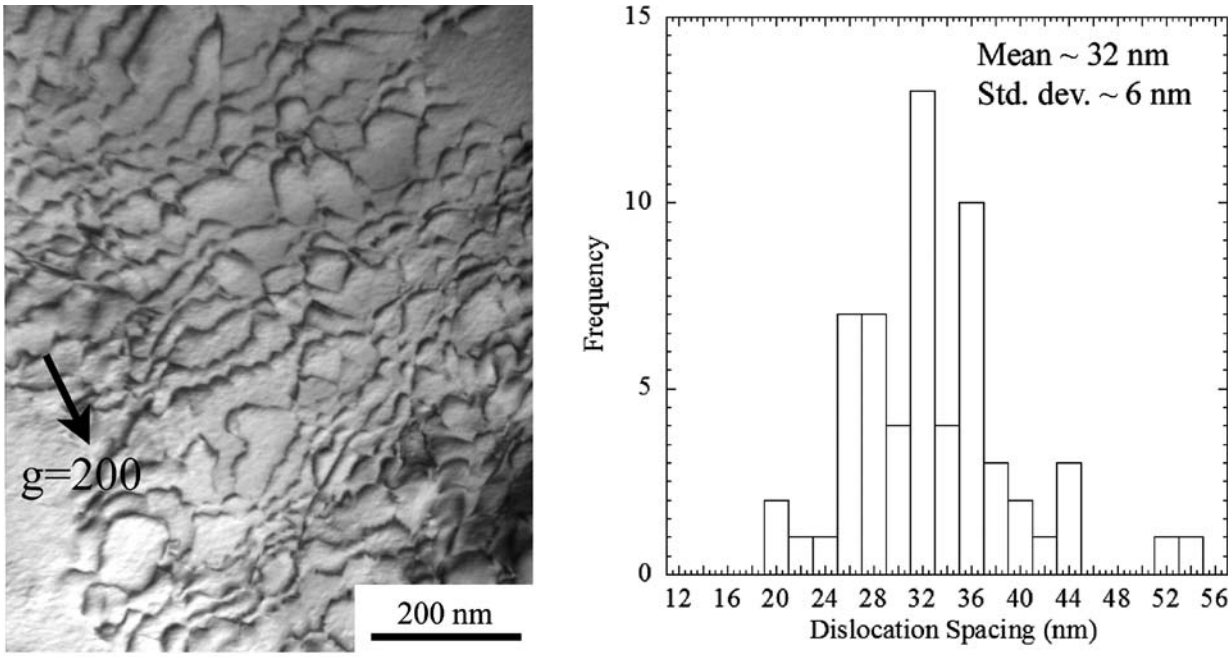

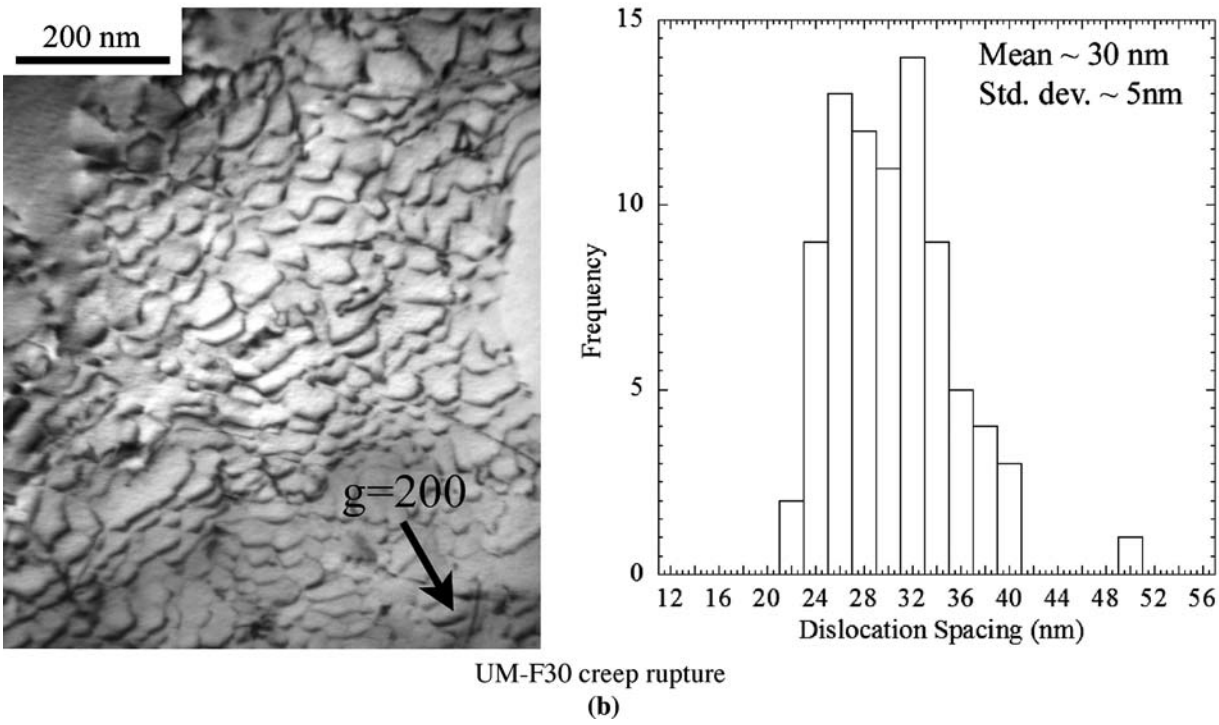

Fig. 10—TEM BF ⟨200⟩-type two-beam images from the (001) zone axis and the distribution of interfacial dislocation spacings in UM-F30 at (*a*) 1 pct creep strain and (*b*) creep rupture at 950 °C and 290 MPa.

who concluded that Co altered the partitioning in Ru-containing alloys with varying levels of Co up to 20 wt pct.[11] Further and more accurate chemical analysis of the phase compositions than the analysis performed on these alloys[12] is necessary to determine the cause of the strongly negative lattice misfit in UM-F20.

As mentioned previously, the morphology of the directionally coarsened precipitates in UM-F22 suggested that the lattice misfit is not as negative as either second- and third-generation commercial superalloys or UM-F19, UM-F20, and UM-F30. The lack of coalescence of the γ' precipitates during prolonged high-temperature exposures at temperatures as high as

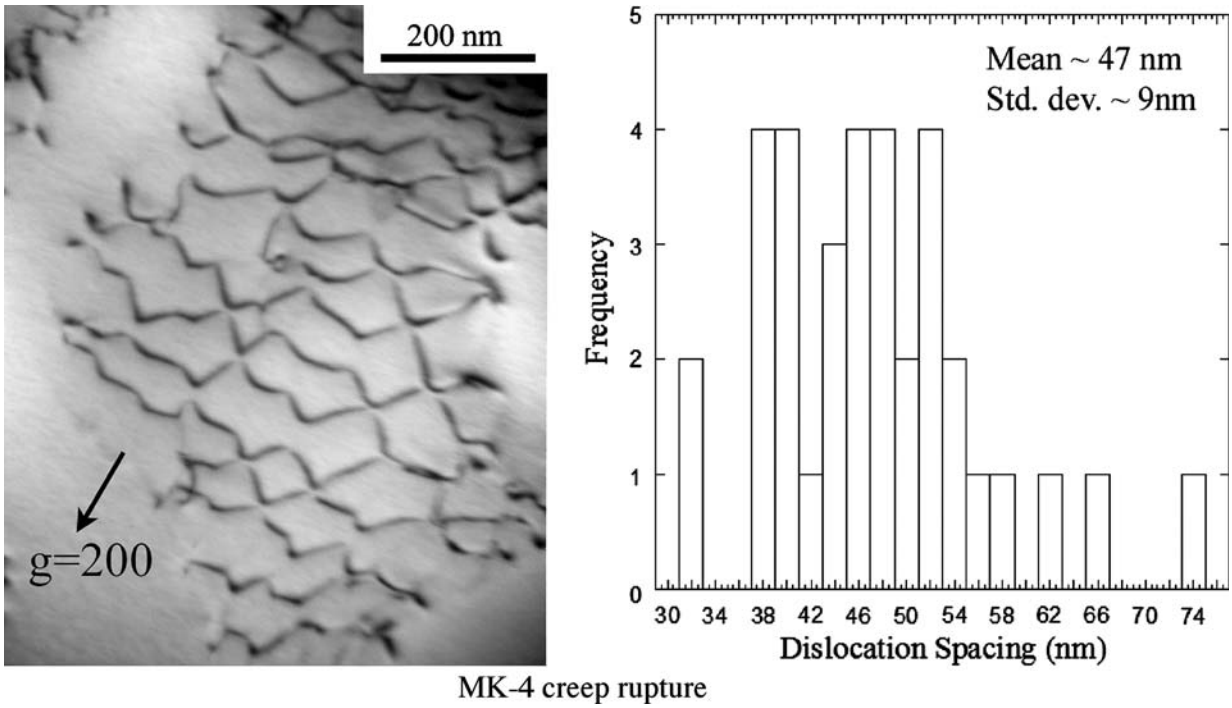

Fig. 11—TEM BF ⟨200⟩-type two-beam images from the (001) zone axis and the distribution of interfacial dislocation spacings in MK-4 creep rupture at 950 °C and 290 MPa.

Table IV. Interfacial Dislocation Network Spacings of UM-F20, UM-F30, and MK-4 at 1 Pct Creep Strain and Creep Rupture*

Alloy	1 Pct Creep Strain	Creep Rupture	Equilibrium
UM-F20	26 nm	24 nm	40 nm
UM-F30	32 nm	30 nm	80 nm
MK-4	—	47 nm	80 nm

*Note: The interfacial dislocation spacings of the equilibrium networks formed during extended exposures at high temperatures with no applied stress are also included.

1050 °C further supports that the lattice misfit is closer to zero than in the other experimental Ru-containing alloys discussed in this article. The lower Cr content, 3.4 wt pct, in UM-F22 is consistent with previous investigations that demonstrate that the combination of Ru and Cr control the lattice misfit in Ru-containing superalloys.[13,27] Furthermore, the rapid directional coarsening kinetics in UM-F20 during high-temperature creep and high-temperature unstressed exposures are consistent with the more negative lattice misfit. It is expected that such variations in high-temperature lattice misfit and phase compositions in these Ru-containing superalloys would have a resultant influence on deformation mechanisms involved in high-temperature creep.

B. *High-Temperature Creep*

The wide range of creep behavior exhibited by the experimental Ru-containing superalloys at 950 °C and 290 MPa is shown in Figure 3 and summarized in Table III. The minimum creep rates vary by more than an order of magnitude, most likely due to the changes in phase composition and misfit. Analysis of the creep resistance of the Ru-containing experimental alloys first requires consideration of the compositional variations that occur within these single-crystal alloys. As mentioned previously, only the amount of Co and Cr vary significantly and the total amount of the solid solution strengtheners, Re, W, and Ta, is nearly equivalent among the experimental alloys. The differences in the amounts of Co and Cr contained in the alloys are not expected to significantly affect the creep resistance, and thus qualitative comparisons between the creep strengths at 950 °C and 290 MPa are justified. Also, recall that the Ru-free reference alloy, MK-4, has a similar total amount of Re, W, and Ta, though the other alloying elements vary from the Ru-containing experimental alloys. In addition to misfit and phase composition, another factor that might influence creep behavior is small variations in the volume fraction of the γ' phase. As shown in Table III, the volume fraction of the γ' phase in these experimental alloys and MK-4 is similar.

The rafting exhibited by negative misfit superalloys contributes to the creep resistance. The dislocation networks that form at the γ-γ' interface are also thought to improve creep resistance by inhibiting dislocation glide through the matrix[19,37,38] and from reaching the interface and then assuming a configuration favorable for shearing of the γ' rafts.[15] The interfacial dislocation networks formed as a result of creep deformation in UM-F20, UM-F30, and MK-4 were denser than the

equilibrium networks that formed to compensate the lattice misfit. This is consistent with other reports of finer dislocation network spacings in crept networks than would be predicted by the magnitude of the lattice misfit.[15,19,39] The importance of the spacing of the crept networks on the creep resistance of these alloys at high temperatures is not well understood, though there has long been discussion of the existence of a relationship between the magnitude of the lattice misfit and the high-temperature mechanical properties. It is generally observed that single-crystal superalloys with a more negative lattice misfit have improved creep resistance, although the exact relationship for high-temperature creep, if one exists, is not well understood. Nevertheless, it has recently been suggested that the spacing within interfacial networks established during creep is proportional to the minimum creep rate and creep rupture lifetime at 1100 °C.[25,40]

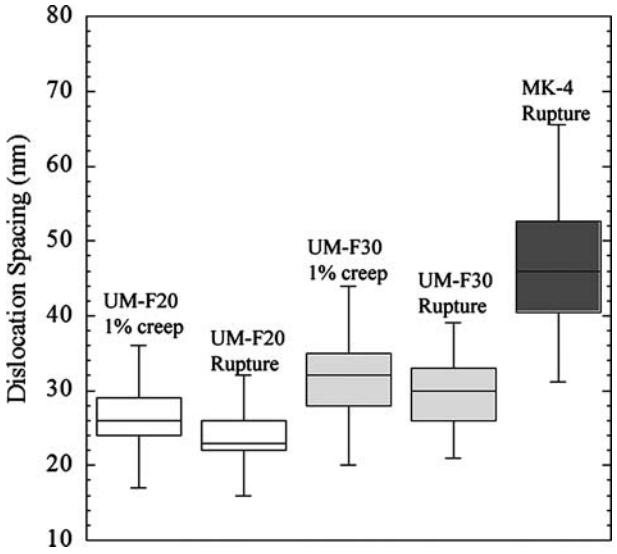

Fig. 12—Box plots showing the distribution of interfacial dislocation spacing measurements in UM-F20 and UM-F30 at both 1 pct creep strain and creep rupture, and MK-4 at rupture. The black line in the distribution represents the median, while the shaded regions encompass the middle 50 pct of the data.

Recall that UM-F22 was much less creep resistant than UM-F20 and UM-F30, and that the lattice misfit of UM-F22 was less negative than UM-F20, UM-F30, and MK-4 (and also UM-F19, based on the solution and aged and crept γ-γ' microstructures). The UM-F30 alloy was significantly more creep resistant than UM-F20 and MK-4, yet the high-temperature lattice misfit of UM-F30 is approximately equal to second-generation commercial alloys, and thus not as negative as in UM-F20.

It is apparent that in this set of alloys the creep rates do not directly scale with the magnitude of the misfit, as illustrated in Figure 16. Although the high-temperature lattice misfits, and therefore equilibrium networks of UM-F30 and MK-4, are similar, the postcrept network spacing in UM-F30 is much finer compared to the postcrept network in MK-4. The crept interfacial network spacing of UM-F30 is nearly as fine as in UM-F20, which has a lattice misfit of –0.65 pct at 950 °C. This suggests that it is more difficult for the dislocations to shear the γ' rafts in UM-F30 compared to MK-4; therefore, extra dislocations accumulate at

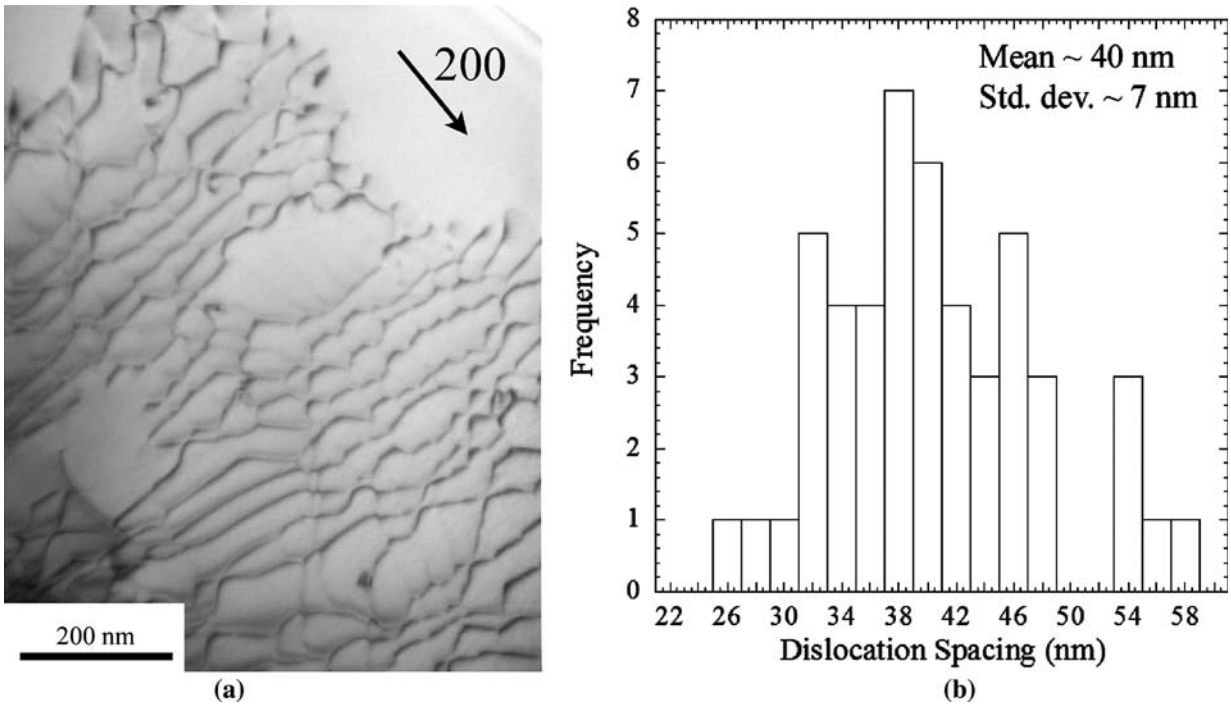

Fig. 13—Typical BF TEM image of the interfacial dislocation network in UM-F20 after 1500 h at 950 °C taken in a ⟨200⟩-type two-beam from the (001) zone axis and the distribution of network spacings after 1500 h at 950 °C.

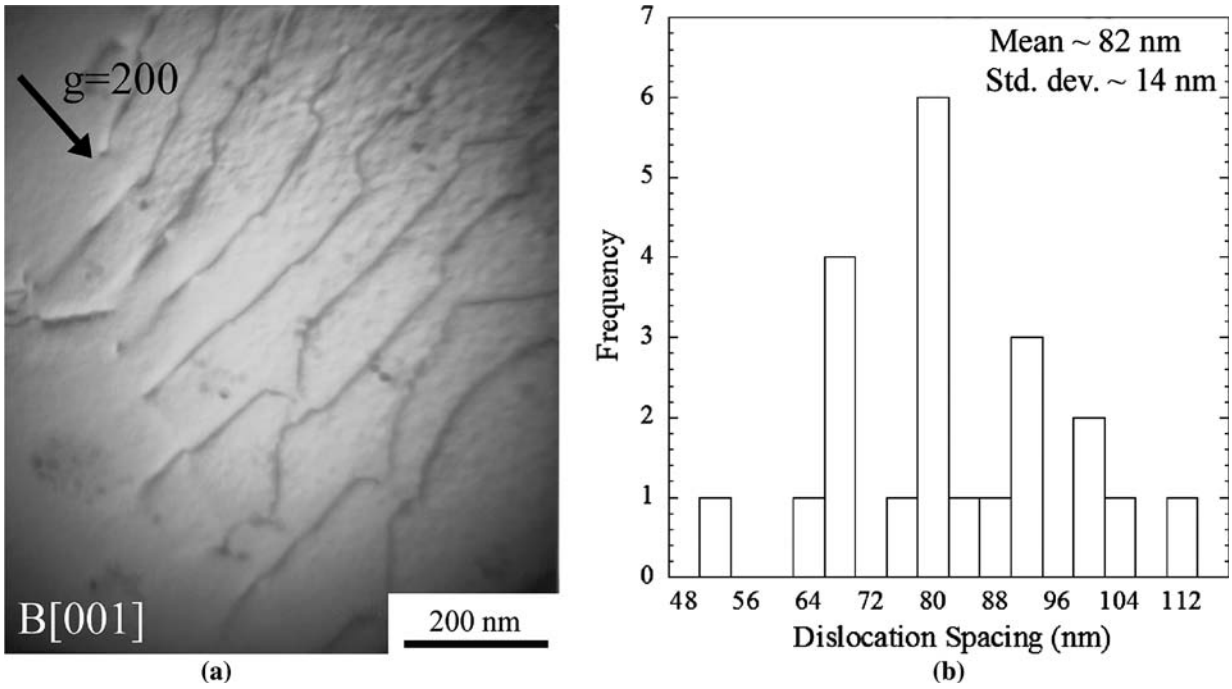

Fig. 14—(*a*) TEM images from a ⟨200⟩-type two-beam condition in the (001) zone axis of a typical interfacial dislocation network in UM-F30 after 1150 h at 1050 °C. (*b*) Histogram of the equilibrium interfacial dislocation network spacings in UM-F30 after 1150 h at 1050 °C.

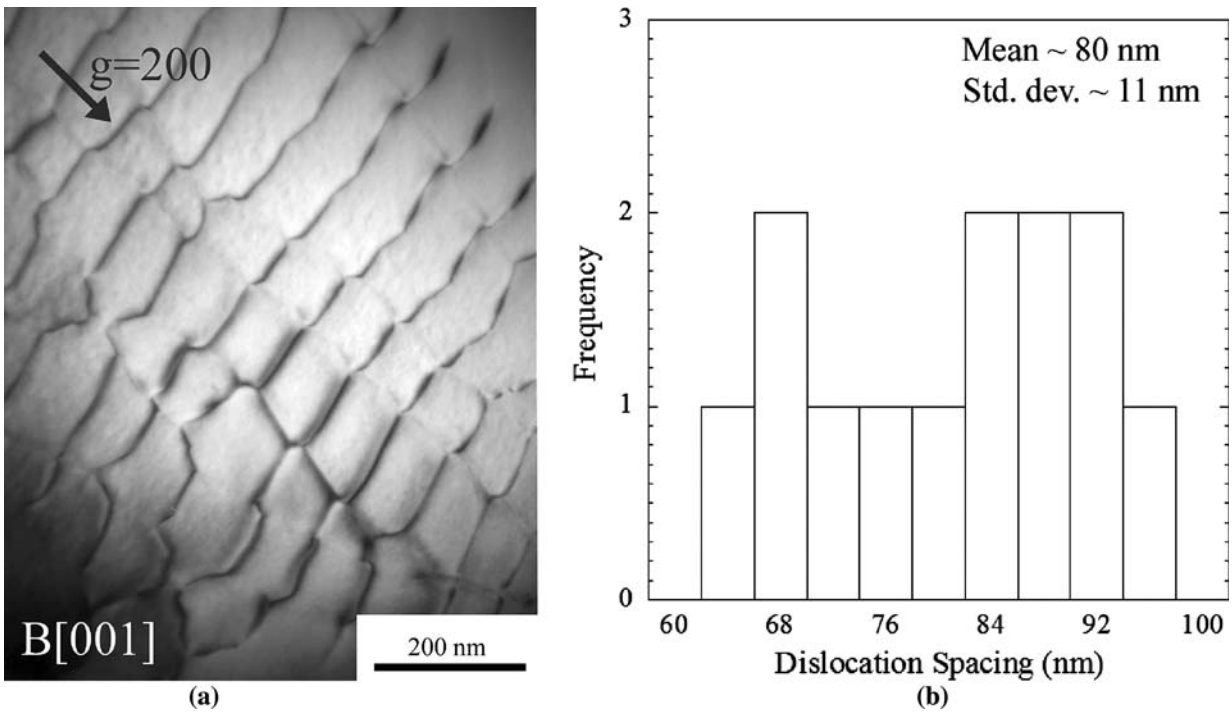

Fig. 15—(*a*) TEM images from a ⟨200⟩-type two-beam condition in the (001) zone axis of a typical interfacial dislocation network in MK-4 after 1150 h at 1050 °C. (*b*) Histogram of the equilibrium interfacial dislocation network spacings in MK-4 after 1150 h at 1050 °C.

the γ-γ' interface in UM-F30. There are fewer extra dislocations (dislocations in excess of those necessary to accommodate the lattice misfit) observed at the interfaces in UM-F20 than in UM-F30, again illustrating the role of the strength of the γ' rafts in the high-temperature creep resistance. These results collectively suggest that the high-temperature creep resistance cannot be predicted by a single factor, such as the lattice misfit. Instead, the balanced strength of the γ and the γ' phases, the lattice misfit, and the interfacial dislocation

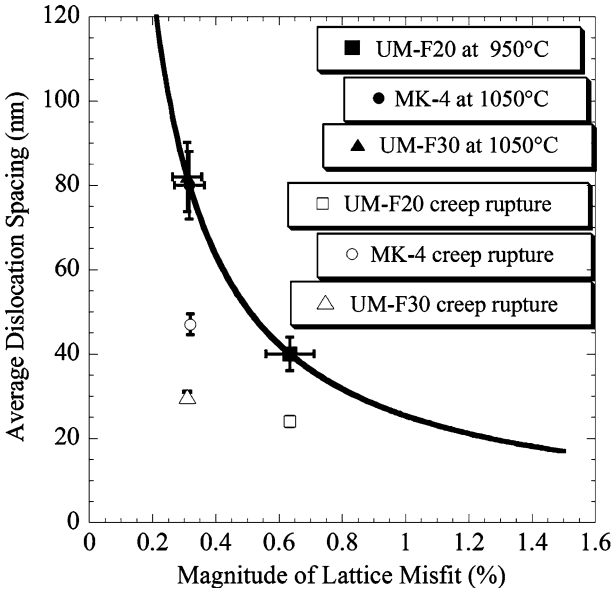

Fig. 16—Plot of the magnitude of the lattice misfit in UM-F20, UM-F30, and MK-4 determined from high-temperature equilibrium network spacings, which include the postcrept network spacings at the corresponding lattice misfit. Error bars represent the 95 pct confidence interval for the mean network spacing or, in the *x*-direction, the corresponding misfits.

networks must be addressed in combination to predict or control the creep resistance of these alloys.

Based on the experimental observations reported here, two possibilities for the rate-controlling mechanism during high-temperature creep of superalloys in the rafting regime can be envisaged: (1) the viscous motion of dislocation pairs through the γ' rafts; and (2) periodic (time-dependent) penetration of dislocations from the interfacial networks into the rafted precipitates. Srinivasan and co-workers have suggested that pairwise cutting can occur within γ' rafts by a combined climb and glide mechanism in CMSX-6 at 1020 °C and 80 MPa.[41] The creep rate is then limited by the viscous motion of the climbing dislocation through the raft. In this case, the experimental creep rate coincided well with the calculated strain rate, based on a model of the viscous shearing. A similar calculation of the creep rate, $\dot{\gamma}$, was performed for the present Ru-containing experimental superalloys using the climb velocity determined by Srinivasan and co-workers:

$$\dot{\gamma} = 0.5\rho b v_c \qquad [3]$$

where ρ is the dislocation density, b is the Burgers vector, and v_c is the climb velocity determined for CMSX-6 as 4×10^{-8} m/s. In reference to that model, the climb forces would be higher in the present work but are offset by the lower self-diffusion coefficient, resulting in a climb velocity that is less than an order of magnitude different. The density of dislocations within the rafts, ρ, was determined from TEM images taken longitudinally in the gage section of UM-F20 after creep rupture, and was determined to be $3 \times 10^{12}/\text{m}^2$. Therefore, the creep rate is estimated as 1.5×10^{-5}/s. The experimentally determined creep rate for UM-F20, however, was several orders of magnitude lower at 6×10^{-9}/s. The considerable difference between the calculated and experimentally determined creep rate suggests that the viscous motion of dislocation pairs through the γ' rafts is not the rate limiting process for this alloy at 950 °C and 290 MPa. This is in contrast to the findings of Srinivasan and co-workers for CMSX-6, in which case the shearing dislocation density was an order of magnitude lower ($10^{11}/\text{m}^2$), resulting in a lower calculated creep rate that matched the experimentally observed rate. In the case of UM-F20, the experimentally observed rate was lower than for CMSX-6 and thus is not consistent with the calculated rate.

The other possibility for the rate limiting creep mechanism is the time-dependent penetration of the dislocations through the interfacial dislocation networks and into the rafts. The time dependence may be a result of either (a) the frequency at which two parallel $a/2\langle 110\rangle$ dislocations arrive at the γ-γ' interface, or (b) the frequency at which a gliding matrix $a/2\langle 110\rangle$ dislocation encounters a compatible $a/2\langle 110\rangle$ network dislocation. The former is unlikely based on the present TEM observations that show excess dislocations present in the matrix channels (Figures 5 through 7). There is a substantial density of gliding matrix dislocations observed bowing through the matrix channels in the experimental alloys, and therefore, the presence of a dislocation of the appropriate Burgers vector is not likely to be a rate limiting concern. This is clearly observed in Figure 7, where matrix dislocations are observed to bow through the γ channels with no evidence of shearing, thus suggesting difficulty in penetrating the network and γ-γ' interface.

The present microscopy studies suggest that the time dependence of penetrating pairs of dislocations is the most likely controlling mechanism for creep in this class of alloys at the conditions evaluated. The network structure is rapidly established along the γ-γ' interfaces during primary creep; further entry of dislocations that sustain the creep process would elicit interactions between the existing network structure and the gliding matrix dislocations. Considering the deposition of a dislocation segment by glide of a matrix $a/2\langle 110\rangle$, it is likely that its position at the interface will lie between two pre-existing network dislocations. If the dislocation is of the correct (similar) sign, climb of this deposited dislocation onto an adjacent glide plane with a network segment would provide the necessary pairwise-cutting source for raft penetration. Note that significant climb has already occurred within the network to achieve a desirable misfit-reducing configuration of the net. Another local climb event of significance would involve dislocations of opposite signs climbing to an adjacent plane in order to annihilate the network dislocation, resulting in a reduction in dislocation density and localized coarsening of the network. Because dislocations entering a channel with an established network have an equal chance of being of similar or opposite sign to neighboring dislocations, the rate of production of dislocation pairs that can shear rafts would be directly related to the rate of coarsening of an established

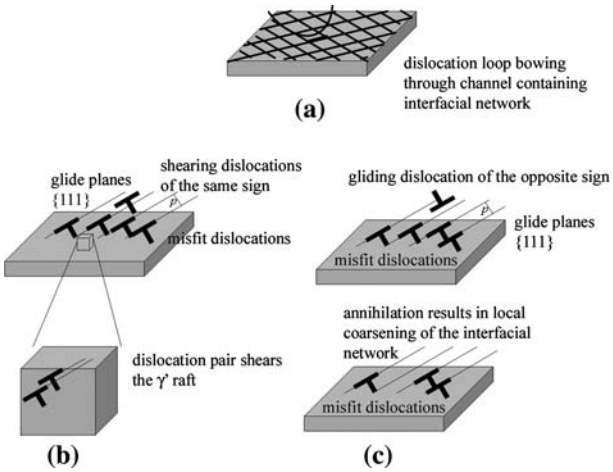

Fig. 17—Schematic illustrating the situation of a gliding dislocation loop bowing in through the network (*a*) of the same sign (*b*) and a gliding dislocation of opposite sign (*c*) encountering the interfacial dislocation network. The dislocation of the same sign results in a shearing event and the approach of a dislocation of opposite sign results in local coarsening of the dislocation network.

network during creep. These two situations are depicted schematically in Figure 17.

Considering that the creep rate is limited by the climb velocity of dislocations into critical shearing configurations at the scale of the interfacial network, then the overall creep rate can be estimated from the following:

$$\dot{\varepsilon} = b\rho\frac{d\bar{x}}{dt} \qquad [4]$$

where ρ is the interfacial dislocation density and $d\bar{x}/dt$ represents the average glide distance per raft shearing event per unit time. The $d\bar{x}/dt$ term will be governed by the climb distance, λ, and climb rate, v_c, of the dislocations at the γ-γ' interface, as well as the width of the raft, β. Thus,

$$\frac{d\bar{x}}{dt} = \frac{\beta}{\lambda}v_c \qquad [5]$$

with climb velocity as

$$v_c = \frac{D\Omega\sigma b}{b^2 \mathrm{k}T} \qquad [6]$$

where D is the diffusivity; Ω is the atomic volume, where $\Omega \approx b^3$; k is the Boltzmann's constant, and T is the temperature.[42] Thus, the creep rate would then be

$$\dot{\varepsilon} = \frac{\rho D\sigma b^3}{\mathrm{k}T}\left(\frac{\beta}{\lambda}\right) \qquad [7]$$

It is necessary to consider only the density of dislocations involved in generating shearing pairs of dislocations from the interfacial network. Thus, only a fraction of the dislocations in the network will experience an interaction with the appropriate type of gliding dislocation; this fraction is designated by a pre-exponential factor, Z

$$\dot{\varepsilon} = \frac{Z\beta\rho D\sigma b^3}{\lambda \mathrm{k}T} \qquad [8]$$

Recent interdiffusion experiments on Ni-Re binary alloys suggest that the interdiffusion coefficient at 950 °C is approximately $D = 6 \times 10^{-18}\,m^2/s$.[43] The density of interfacial dislocations is approximately $10^{15}/m^2$, while $\beta/\lambda \approx 10$ for the present alloys. The stress, σ, is approximately 290 MPa in the present experiments. Considering a creep rate of approximately 10^{-8}/s, an estimate of the pre-exponential factor, Z, on the order of 10^{-6} is obtained. Not surprisingly, this suggests that only a few segments of the dislocations within the interfacial network are involved in the accumulation of strain during high-temperature creep. So it is worth considering the spacing between such active links in the network present with density ρ_{act}. With $Z \approx 10^{-6}$, approximately one dislocation out of every 10^6 of the network dislocations is active. This spacing between active links should be of the same order of magnitude as observed in Figure 6 and the spacing that is calculated from the density of dislocation pairs in the γ' rafts, $10^{12}/m^2$, which corresponds to approximately 1 dislocation pair shearing the raft per 1 μm. The fraction of active dislocations was determined from the experimental spacing between shearing events and the interfacial dislocation spacing as approximately 5×10^{-4}, quite similar to the calculated value, Z, which was approximately 10^{-6}.

It has long been recognized that the creep stress exponent for superalloys is higher than would be predicted from conventional theories for creep in single-phase materials. Viewing the preceding creep rate equation, this is most likely to be due to the variation of Z and ρ with applied stress and the associated difficulty of shearing the γ' precipitates. To date, there has been very limited investigation of the role of interfacial dislocation networks and their relationship to frequency of precipitate shearing events as a function of stress. A more fully developed constitutive equation for creep requires a more detailed understanding of how the interfacial dislocation network spacing adjusts with applied stress and with increasing densities of dislocations gliding through the matrix channels. The fact that excess dislocations beyond the density required to relax misfit are present is consistent with the possibility that the higher order stress dependence would arise from these interfacial dislocation phenomena. It would also be beneficial to determine how the frequency of γ' shearing events varies with applied stress and the composition of the γ', while the lattice misfit and interfacial network spacing remain constant.

To summarize, creep deformation of single-crystal superalloys in the directional coarsening regime is a complex process, governed by a number of interdependent microstructural parameters. Ruthenium additions, in combination with variation in Cr and Co, provide a unique opportunity to vary lattice misfit without removal of slow-diffusing strengthening refractory additions (Re and W). It is clear that neither the magnitude of the lattice misfit, nor the densities of dislocations in

the interfacial networks are the sole contributor to the measured creep resistance. The present study suggests that precipitate morphology, lattice misfit, crept dislocation network spacings, and a balance between the individual strengths of the γ and the γ' phase are all important to achieving high creep resistance. The most creep-resistant nickel-base superalloy would have a negative lattice misfit that was of a large enough magnitude (0.25 to 0.3 pct) to facilitate the rapid development of a rafted microstructure during high-temperature creep. Beyond this a high resistance of the γ' phase to shearing is important. An alloy that has a high precipitate shearing resistance will accumulate excess matrix dislocations. A high precipitate shearing resistance will, in turn, be dependent on precipitate composition and the associated anti-phase boundary and complex fault energies. Finally, a slow interdiffusion coefficient in the matrix will slow the climb kinetics in the near interfacial regime. These chemical traits are, apparently, achieved *via* high refractory alloy content in both the γ and γ' phases.

V. CONCLUSIONS

1. The interfacial dislocation network spacings at 1 pct creep were consistent with the spacings measured after creep deformation to rupture, suggesting that the interfacial network spacings are relatively constant after their formation during primary creep.
2. The high-temperature lattice misfits determined from the spacings of the equilibrium dislocation networks suggest that Ru-containing superalloys can have a wide range of lattice misfits, as large as –0.65 pct.
3. The most creep-resistant Ru-containing experimental superalloy did not have the finest interfacial dislocation networks following creep, nor did it have the most negative lattice misfit, suggesting that at 290 MPa and 950 °C the creep resistance is controlled by a balance of properties including the strength of the γ and the γ' phase and the interfacial dislocation networks.
4. The rate-limiting step during high-temperature creep deformation is most likely the climb of matrix dislocations into configurations that can shear the ordered, high-strength γ' rafts.

ACKNOWLEDGMENTS

The authors gratefully acknowledge the National Science Foundation, Alstom Power, and the Air Force Research Laboratory for financial support of this research.

REFERENCES

1. H. Murakami, T. Honma, Y. Koizumi, and H. Harada: *Superalloys 2000*, Seven Springs, PA, 2000, T.M. Pollock, R.D. Kissinger, R.R. Bowman, K.A. Green, M. McLean, S. Olson, and J.J. Schirra, eds., TMS, Warrendale, PA, 2000, pp. 747–56.
2. K.S. O'Hara, W.S. Walston, E.W. Ross, and R. Darolia: U.S. Patent No. 5,482,789, General Electric Company, Cincinnati, OH, 1996.
3. P. Caron: *Superalloys 2000*, Seven Springs, PA, 2000, T.M. Pollock, R.D. Kissinger, R.R. Bowman, K.A. Green, M. McLean, S. Olson, and J.J. Schirra, eds., TMS, Warrendale, PA. 2000, pp. 737–46.
4. A.C. Yeh and S. Tin: *Parsons 2003: Engineering Issues in Turbine Machinery, Power Plant and Renewables*, A. Strang, R.D. Conroy, W.M. Banks, M. Blackler, J. Leggett, G.M. McColvin, S. Simpson, M. Smith, F. Starr, and R.W. Vanstone, eds., Trinity College, Dublin, Ireland, 2003, TMS, Warrendale, PA, 2003, pp. 673–86.
5. Q. Feng, T.K. Nandy, S. Tin, and T.M. Pollock: *Acta Mater.*, 2003, vol. 51, pp. 269–84.
6. J.X. Zhang, T. Murakumo, H. Harada, and Y. Koizumi: *Scripta Mater.*, 2003, vol. 48, pp. 287–93.
7. S. Tin, A.C. Yeh, A.P. Ofori, R.C. Reed, S.S. Babu, and M.K. Miller: *Superalloys 2004*, Seven Springs, PA, 2004, K.A. Green, T.M. Pollock, H. Harada, T.E. Howson, R.C. Reed, J.J. Schirra, and S. Walston, eds., TMS, Warrendale, PA, 2004, pp. 735–41.
8. T. Yokokawa, M. Osawa, K. Nishida, T. Kobayashi, Y. Koizumi, and H. Harada: *Scripta Mater.*, 2003, vol. 49, pp. 1041–46.
9. R.C. Reed, A.C. Yeh, S. Tin, S.S. Babu, and M.K. Miller: *Scripta Mater.*, 2004, vol. 51 (4), pp. 327–31.
10. A. Volek, F. Pyczak, R.F. Singer, and H. Mughrabi: *Scripta Mater.*, 2005, vol. 52, pp. 141–45.
11. S. Walston, A. Cetel, R. MacKay, K. O'Hara, D. Duhl, and R. Dreshfield: *Superalloys 2004*, Seven Springs, PA, 2004, K.A. Green, T.M. Pollock, H. Harada, T.E. Howson, R.C. Reed, J.J. Schirra, and S. Walston, eds., TMS, Warrendale, PA, 2004, pp. 15–24.
12. L.J. Carroll, Q. Feng, J.F. Mansfield, and T.M. Pollock: *Mater. Sci. Eng. A*, 2007, vol. 457, pp. 292–99.
13. L.J. Carroll, Q. Feng, J.F. Mansfield, and T.M. Pollock: *Metall. Mater. Trans. A*, 2006, vol. 37A, pp. 2927–38.
14. M. Fährmann, W. Hermann, E. Fährmann, A. Boegli, T.M. Pollock, and H.G. Sockel: *Mater. Sci. Eng. A*, 1999, vol. 260, pp. 212–21.
15. T.M. Pollock and R.D. Field: in *Dislocation in Solids*, F.R.N. Nabarro and M.S. Duesbery, eds., Elsevier Science B.V., Amsterdam, Netherlands, 2002, vol. 11, pp. 593–95.
16. A. Lasalmonie and J.L. Strudel: *Philos. Mag.*, 1975, vol. 32, pp. 937–49.
17. D.F. Lahrman, R.D. Field, R. Darolia, and H.L. Fraser: *Acta Metall.*, 1988, vol. 36 (5), pp. 1309–20.
18. T.P. Gabb, S.L. Draper, D.R. Hull, R.A. MacKay, and M.V. Nathal: *Mater. Sci. Eng. A*, 1989, vol. 118, pp. 59–69.
19. M. Feller-Kniepmeier and T. Link: *Mater. Sci. Eng. A*, 1989, vol. 113, pp. 191–95.
20. N. Miura, Y. Kondo, and N. Ohi: *Superalloys 2000*, Seven Springs, PA, 2000, T.M. Pollock, R.D. Kissinger, R.R. Bowman, K.A. Green, M. McLean, S. Olson, and J.J. Schirra, eds., TMS, Warrendale, PA, 2000, pp. 377–85.
21. R.A. MacKay and L.J. Ebert: *Superalloys*, Seven Springs, PA, 1984, M. Gell, C.S. Kortovich, R.H. Bricknell, W.B. Kent, and J.F. Radavich, eds., TMS, Warrendale, PA, 1984, pp. 135–44.
22. M.V. Nathal and L.J. Ebert: *Superalloys*, Seven Springs, PA, 1984, M. Gell, C.S. Kortovich, R.H. Bricknell, W.B. Kent, and J.F. Radavich, eds., TMS, Warrendale, PA, 1984, pp. 125–33.
23. T.M. Pollock, R.D. Field, and W.H. Murphy: *Modelling of Microstructural Evolution in Creep Resistant Materials*, Imperial College of Science, London, 1998, pp. 193–212.
24. M.V. Nathal, R.A. MacKay, and R.V. Miner: *Metall. Trans. A*, 1989, vol. 20A, pp. 133–40.
25. J.X. Zhang, T. Murakumo, Y. Koizumi, T. Kobayashi, H. Harada, and S. Masaki, Jr.: *Metall. Mater. Trans. A*, 2002, vol. 33A, pp. 3741–46.
26. J.X. Zhang, T. Murakumo, H. Harada, Y. Koizumi, and T. Kobayashi: *Superalloys 2004*, Seven Springs, PA, 2004, K.A. Green, T.M. Pollock, H. Harada, T.E. Howson, R.C. Reed, J.J. Schirra, and S. Walston, eds., TMS, Warrendale, PA, 2004, pp. 189–95.
27. L.J. Rowland, Q. Feng, and T.M. Pollock: *Superalloys 2004*, Seven Springs, PA, 2004, K.A. Green, T.M. Pollock, H. Harada, T.E. Howson, R.C. Reed, J.J. Schirra, and S. Walston, eds., TMS, Warrendale, PA, 2004, pp. 697–706.

28. M. Konter, M. Newnham, and C. Tonnes: U.S. Patent No. 5,759,301, ABB Research Ltd., Zurich, Switzerland, 1998.
29. K. Harris and G.L. Erickson: U.S. Patent No. 4,643,782, Cannon Muskegon Corporation, Muskegon, MI, 1987.
30. A.C. Yeh and S. Tin: *Scripta Mater*., 2005, vol. 52, pp. 519–24.
31. W. Schneider, J. Hammer, and H. Mughrabi: *Superalloys 1992*, Seven Springs, PA, 1992, S.D. Antolovich, R.W. Stusrud, R.A. MacKay, D.L. Anton, T. Khan, R.D. Kissinger, and D.L. Klarstrom, eds., TMS, Warrendale, PA, 1992, pp. 589–98.
32. L.J. Rowland: Ph.D. Thesis, University of Michigan, Ann Arbor, MI, 2005, pp. 1–237.
33. A. Fredholm and J.L. Strudel: *Superalloys 1984*, Seven Springs, PA, M. Gell, C.S. Kortovich, R.H. Bricknell, W.B. Kent, and J.F. Radavich, eds., TMS, Warrendale, PA, 1984, pp. 211–20.
34. M.V. Nathal and L.J. Ebert: *Metall. Mater. Trans. A*, 1985, vol. 16A, pp. 1863–70.
35. R. Volkl, U. Glatzel, and M. Feller-Kniepmeier: *Acta Mater*., 1998, vol. 46 (12), pp. 4395–4404.
36. Schulze and M. Feller-Kniepmeier: *Mater. Sci. Eng. A*, 2000, vol. 281, pp. 204–12.
37. T.M. Pollock and A.S. Argon: *Acta Metall. Mater*., 1992, vol. 40 (1), pp. 1–30.
38. W. Schneider, J. Hammer, and H. Mughrabi: *Superalloys 1992*, Seven Springs, PA, S.D. Antolovich, R.W. Stusrud, R.A. MacKay, D.L. Anton, T. Khan, R.D. Kissinger, and D.L. Klarstrom, eds., TMS, 1992, pp. 589–98.
39. T.P. Gabb, S.L. Draper, D.R. Hull, R.A. MacKay, and M.V. Nathal: *Mater. Sci. Eng. A*, 1989, vol. A118, pp. 59–69.
40. J.X. Zhang, T. Murakumo, Y. Koizumi, and H. Harada: *J. Mater. Sci*., 2003, vol. 38, pp. 4883–88.
41. R. Srinivasan, G.F. Eggeler, and M.J. Mills: *Acta Mater*., 2000, vol. 48, pp. 4867–78.
42. J.P. Hirth and J. Lothe: *Theory of Dislocations*, John Wiley & Sons, New York, NY, 1982.
43. M.S.A. Karunaratne, P. Carter, and R.C. Reed: *Mater. Sci. Eng*., 2000, vol. A281, pp. 229–33.